

ARTICLE

A general approach to multicomponent metal-decorated crumpled reduced graphene oxide nanocomposites using a flame-based process

Received 00th January 20xx,
Accepted 00th January 20xx

DOI: 10.1039/x0xx00000x

Mohammad Moein Mohammadi,^a Shikuan Shao,^a Santosh Srivatsa Gunturi,^a Anirudh Ravi Raghavan,^a Naveshkaanth Alexander,^a Christopher M. Stafford,^b Raymond D. Buchner,^a and Mark T. Swihart,^{*a}

We introduce a general approach for synthesizing multicomponent metal-decorated crumpled reduced graphene oxide nanocomposites using a one-step, continuous flame-based process. Crumpled reduced graphene oxide Balls (CGB) were produced from Graphene Oxide (GO) in a High Temperature Reducing Jet (HTRJ) reactor. Moreover, CGBs were simultaneously decorated with different transition metal nanoparticles, including cobalt (Co), nickel (Ni), iron (Fe), and palladium (Pd). Various alloy metal-decorated crumpled reduced graphene oxide Balls (M-CGBs) including CoPd-, CoNi-, CoPdNi-, and CoNiFe-CGBs were successfully synthesized using a general recipe. The key advantage of the HTRJ system over common flame-based aerosol synthesis methods is the separation of flame and product formation zones, which allows production and/or reduction of nanomaterials that can be reduced by H₂ in the presence of H₂O. Nanomaterials are produced from aqueous precursors containing low-cost metal salts and dispersed GO. Electron microscopy and other characterization methods show the decoration of the CGBs with sub-4 nm diameter binary and ternary alloy, non-oxide transition metal nanoparticles of controlled compositions. The nanostructures made by this process can potentially be used as electrocatalysts for fuel cells, electrodes in batteries and supercapacitors, conductive inks for printed electronics, catalysts in wastewater treatment, and many other applications where a graphitized carbon-metal nanomaterial is needed.

Introduction

In the last decade, three-dimensional (3D) graphene nanostructures have drawn enormous attention due to their fast ion and electron transport, reduced restacking, high stability, and excellent mechanical strength.^{1, 2} These nanostructures are remarkably aggregation-resistant in both solution and in the solid state and do not collapse or unfold during common processing steps.³ Therefore, interest in studying and designing new nanostructures based on 3D graphene nanomaterials and investigating their performance in different applications has grown rapidly. To date, they have been utilized as lithium ion battery anodes,⁴ supercapacitor electrodes,⁵ electrocatalysts for oxygen reduction and evolution reactions,⁶ biosensors,⁷ and counter electrodes in dye sensitized solar cells.⁸

These unique 3D graphene architectures can be produced by template-assisted,⁹ aerosol-based,¹⁰ and solution synthesis methods.¹¹ In template-assisted methods, initially, another compound is used as a core material followed by graphene formation on the core. Eventually, the core is removed and 3D spherical

graphene materials remain.¹² In the solution synthesis methods including the solvothermal method, several steps are usually required to make 3D crumpled graphene-based materials.¹³ Unlike the two abovementioned methods, aerosol-based techniques offer one-step, continuous synthesis of crumpled 3D graphene micro- and nanomaterials without the need of additional compounds.¹ In this method, a graphene oxide (GO) aqueous dispersion is usually used as the precursor and is atomized to form an aerosol. The aerosol droplets enter a high-temperature zone where GO sheets crumple due to the capillary force associated with rapid evaporation of water.¹⁴ The spray pyrolysis technique is usually employed to make such crumpled graphene balls.¹⁵ This method is mostly used only for crumpling of GO sheets, not for reducing them. It has its own limitations such as usually low production rates, formation of large particles *via* a droplet-to-particle synthesis route, and low potential for commercialization compared to other aerosol processes.¹⁶ Flame aerosol technology is an ideal technique for the rapid and scalable synthesis of nanomaterials. For instance, carbon black, another carbonaceous material, is produced by this method at industrial scale (millions of tons per year).¹⁷ However, as far as we know, no one has synthesized 3D graphene-based nanomaterials using a flame process. We have developed a flame-based process in our group that decouples flame chemistry and particle-formation chemistry to enable production of nanomaterials at high temperatures in the absence of oxygen.

^a Department of Chemical and Biological Engineering, University at Buffalo, The State University of New York, Buffalo, NY 14260, USA.

^b Materials Science and Engineering Division, National Institute of Standards and Technology, Gaithersburg, MD 20899, USA.

* Corresponding author: swihart@buffalo.edu

Electronic Supplementary Information (ESI) available: Additional electron microscopy images of metal-decorated crumpled reduced graphene oxide balls, equilibrium constant calculations for metal reduction in the presence of water, and additional XPS data for the samples]. See DOI: 10.1039/x0xx00000x

3D graphene nanomaterials are often integrated with other compounds for specific applications. For instance, the addition of

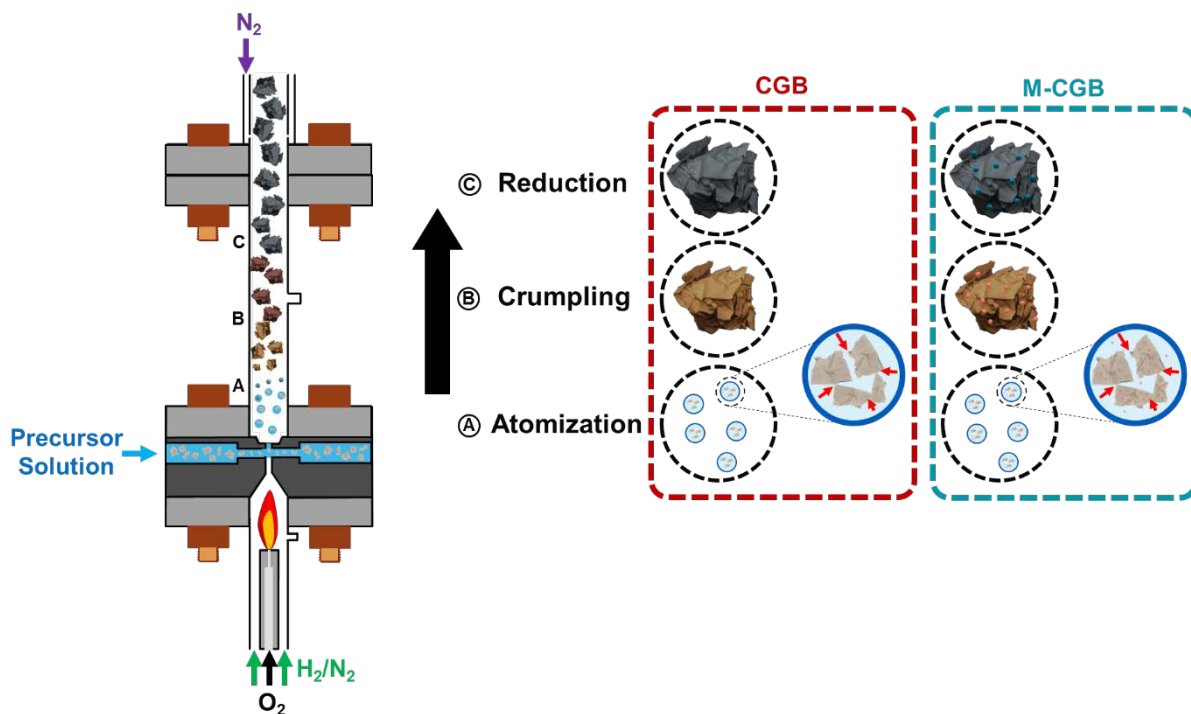


Fig. 1 Schematic of nanoparticle formation in the HTRJ process (CGB: Crumpled Graphene Ball, M-CGB: Metal-decorated Crumpled Graphene Ball)

different metal and metal oxide nanoparticles to a graphitic carbon usually boosts performance in electrocatalytic applications.¹⁸ To date, various transition metal-decorated crumpled graphene balls have been reported. A few studies have reported crumpled graphene-supported noble metal nanocomposites such as graphene-based hybrid nanostructures of : Pt-Ir,¹⁹ Pd,²⁰ Pt,²¹ and Ag.²² On the contrary, the synthesis of non-noble transition metal-3D graphene hybrid structures is challenging and area. These metals, including Co, Ni, and Fe, are harder to reduce to their zerovalent metallic state compared to the noble metals. Lee et al. reported the aerosol synthesis of crumpled graphene decorated with Fe-Co oxides nanoparticles. To achieve the final product, another post-treatment of nanomaterials was needed to convert metal hydroxides to metal oxides.²³ Gao et al. presented zinc oxide-decorated crumpled reduced GO nanomaterials prepared by an ultrasonic spray pyrolysis method.²⁴ Lee et al. produced 3D graphene loaded with hematite (Fe_2O_3) and magnetite (Fe_3O_4) nanostructures by varying the process parameters of an aerosol spray pyrolysis method.²⁵ Fan et al. made Co_3O_4 /crumpled graphene microspheres using what they termed an aerosol-assisted frying process.²⁶ To the best of our knowledge, to date, there is no report on the synthesis of pure non-oxide, non-noble transition metal-3D graphene hybrid nanocomposites.

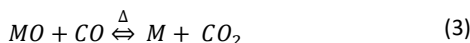
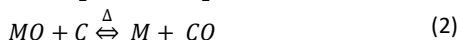
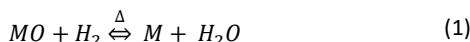
Herein, we present the one-step, continuous synthesis of 3D graphene nanostructures using a flame-based process. Moreover, we simultaneously decorate these nanostructures with different transition metal nanoparticles. We demonstrated the synthesis of crumpled reduced graphene oxide balls (CGBs) and multicomponent Metal (Co, Ni, Fe, Pd)-decorated Crumpled reduced Graphene oxide Balls (M-CGBs) using a flame-driven High Temperature Reducing Jet

(HTRJ) process. M-CGBs of different chemical compositions were made by injecting aqueous solutions of low-cost metal salt precursors containing dispersed GO into the reactor. M-CGBs prepared in this study include binary (CoNi and CoPd) and ternary (CoNiFe and CoNiPd) alloy nanoparticle-decorated CGBs. Multiple characterization techniques showed the generality and reproducibility of this technique for the synthesis of various M-CGBs. CGBs have great potential in applications in which a 3D partially-reduced GO is needed. In addition, using a general recipe, different transition metal nanoparticles can be decorated on the CGBs to optimize them for particular applications.

Results and discussion

Fig. 1 shows a schematic of CGB and M-CGB formation in the HTRJ process. GO sheets self-assembled into crumpled balls due to capillary compression driven by rapid evaporation of the droplets. Each ball may contain one or more GO sheets. After crumpling, due to the presence of excess hydrogen at high temperature, oxygen-containing groups on GO were reduced, producing CGBs. In the case of M-CGBs, aerosol droplets contain both GO and metal precursor ions. Metal ions may be adsorbed on GO sheets in solution via electrostatic interactions. During the solvent evaporation and crumpling, metal nanocrystals grow from metal ions and assemble on both external and internal surfaces of the CGBs.²⁹ Metal oxide

nanocrystals are further reduced in the reaction chamber by the graphitized carbon, produced carbon monoxide, and excess hydrogen at high temperature according to reactions like those written below, with appropriate changes in stoichiometry for each metal oxide:



As a representative example, we have calculated equilibrium constants of the three above reactions for Co at different temperatures. As shown in **Fig. S1**, CoO can be reduced to Co by hydrogen in the presence of water at temperatures above about 500 K. On the other hand, the reduction of CoO by graphitized carbon is more favorable at higher temperatures (above 900 K). Although the reaction chamber is kept at ~550–600 °C, the temperature at the throat section of the nozzle is closer to the flame temperature and favors the reduction of Co by graphitized carbon. The reduction of CoO by carbon monoxide is favorable at low temperatures. However, the amount of carbon monoxide produced by the reduction of CoO by carbon is likely to be negligible.

Fig. 2 displays the overall morphology of CGBs and M-CGBs made in the HTRJ process. **Fig. 2a** shows a photograph of the CGBs. Unlike GO-based materials that are in brown to dark brown in color, these fluffy CGB powders are black (more similar to graphene) and are not dispersible in water. We attribute this behavior to the reduction of hydroxyl groups on the surface. **Fig. 2b** presents a Scanning Electron Microscopy (SEM) image of the CGBs. As shown in this image, powders are in the form of crumpled structures. Smaller crumpled nanopowders agglomerate and form larger micron-size structures. A Transmission Electron Microscopy (TEM) image of CGBs is shown in **Fig. 2c**. As seen in that image, GO sheets form 3D crumpled structures in the reaction chamber. The size of each crumpled ball depends on the size and the number of GO sheets present in each aerosol droplet. To demonstrate the concept of one-step metal-decoration, morphologies of the CGB-supported cobalt-nickel alloy nanoparticles (Co:Ni 50:50 mass%) are presented in **Fig. 2d-j**. An SEM image of CoNi-CGBs is displayed in **Fig. 2d**. There is no obvious difference in the crumpling of the CoNi-CGBs compared to the CGBs. The nanocomposites adopted the same crumpled structures with or without the metal-decoration. **Fig. 2e** provides a TEM image of CoNi-CGB deposited directly onto the grid from the product aerosol. The CGB is fully covered by metal nanoparticles with minimal agglomeration compared to typical agglomerated products of aerosol processes. This pattern of metal-decoration suggests that metal nanocrystals grow from metal ions on the surface of GO sheets, perhaps having been adsorbed on the GO sheets in the precursor solution. If metal nanoparticles nucleated from the gas phase, we would expect them to form dendritic or fractal aggregates, rather than being dispersed uniformly on the GO surface. **Fig. 2f** presents a higher magnification TEM image of CoNi-CGB. Nanoparticles are below 4 nm in diameter, as shown by the particle size distribution in **Fig. 2g**. The geometric mean diameter of the 196

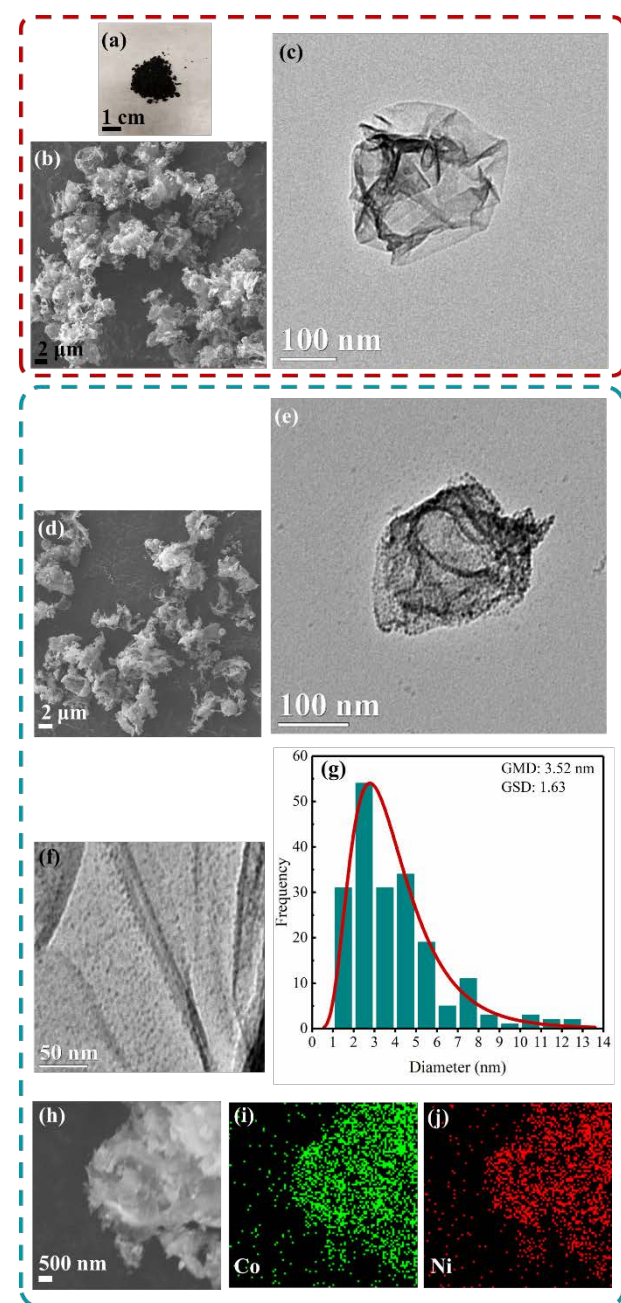


Fig. 2 **a)** Photograph of CGB powders; **b)** SEM image of CGB; **c)** TEM image of CGB; **d)** SEM image of CoNi (50:50 mass%)-CGB; **e)** TEM image of CoNi (50:50 mass%)-CGB; **f)** higher magnification TEM image of CoNi (50:50 mass%)-CGB; **g)** particle size distribution of CoNi (50:50 mass%)-CGB based on the TEM image; **h)** SEM image of CoNi (50:50 mass%)-CGB; Elemental mapping of **(i)** cobalt, and **(j)** nickel in the selected SEM image. In **(g)**, GMD: Geometric Mean Diameter, GSD: Geometric Standard Deviation.

particles counted is 3.52 nm. **Fig. 2h-j** show an SEM image and the corresponding elemental maps of Co and Ni, respectively. The morphologies of other M-CGBs are presented in **Fig. S2-4**.

Fig. 3 presents the X-Ray Diffraction (XRD) patterns of GO, CGB, and M-CGB samples. The XRD patterns of metal-free samples are displayed in **Fig. 3a**. For comparison, the XRD pattern of graphite is

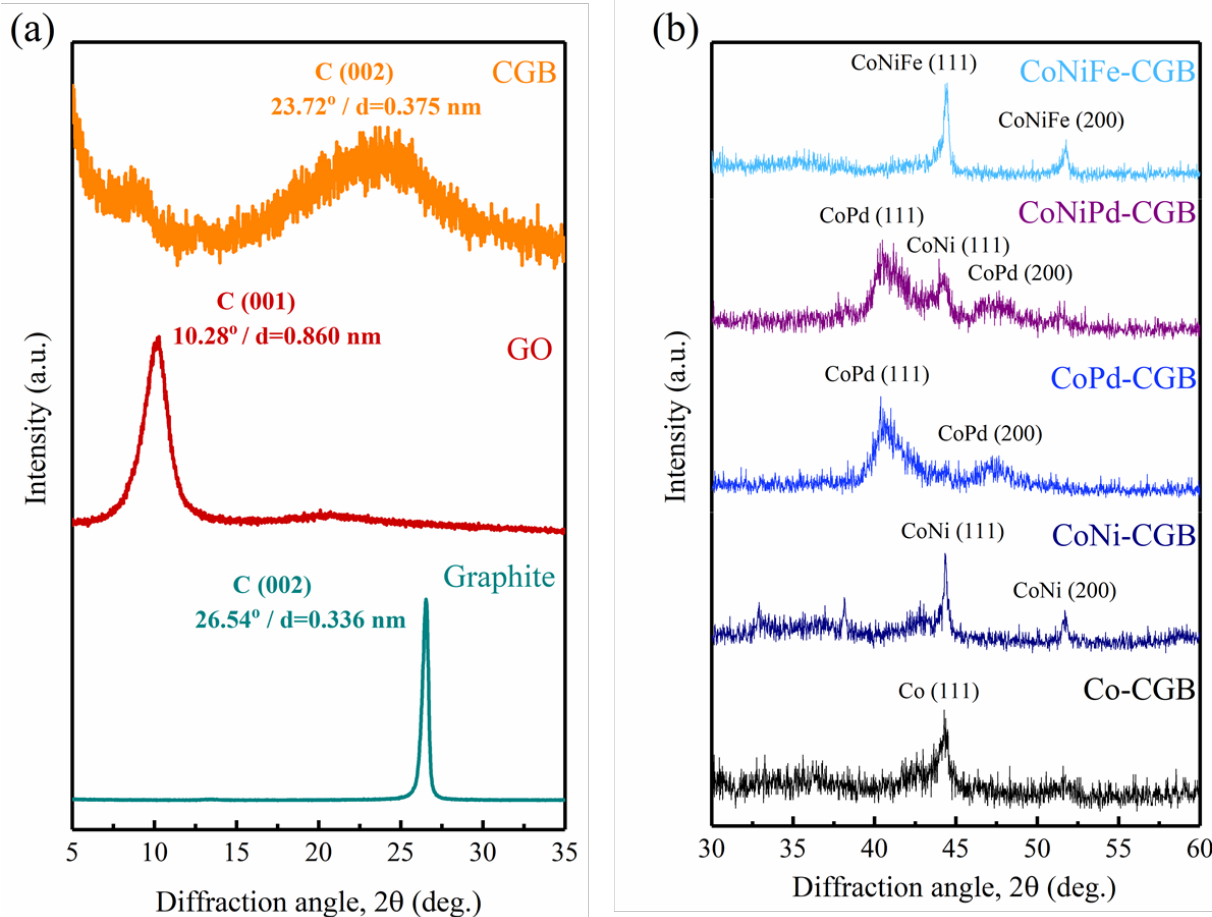


Fig. 3 **a**) XRD patterns of graphite, graphene oxide (GO), and crumpled graphene balls (CGB); **b**) XRD patterns of metal-decorated graphene balls (M-CGBs): Co-CGB, CoNi (50:50 mass%)-CGB, CoPd (50:50 mass%)-CGB, CoNiPd (33:33:34 mass%)-CGB, CoNiFe (33:33:34 mass%)-CGB.

included as well. The GO has a sharp peak at 10.28° attributed to diffraction from C (001) planes with a corresponding d -spacing of 8.60 \AA . After thermal reduction in the HTRJ, the sharp GO peak disappears in the CGB samples. Instead, there is a broad peak between 20° - 25° . Compared to the sharp C (002) graphite peak at 26.54° , this broad peak with its maximum at 23.72° indicates that the stacking of rGO sheets in the CGBs is irregular, with a broad distribution of lamellar spacings. In addition, the average d -spacing of 3.75 \AA is higher than that of graphite (3.36 \AA), reflecting higher average interlamellar spacing. **Fig. 3b** displays the XRD patterns of a series of M-CGBs including Co-CGB, binary CoNi-CGB, and CoPd-CGB, ternary CoNiPd-CGB, and CoNiFe-CGB. The XRD of Co-CGB has a peak at 44.28° in the range of 30 - 60° which corresponds to the FCC Co (111) planes. For CoNi-CGB, the first peak has slightly shifted to 44.32° which is between the peak positions for Co (111) and Ni (111). The second peak attributed to the CoNi (200) is at 51.70° . The first peak shift suggests the formation of CoNi alloys on the CGBs and can be compared to the FCC CoNi reference pattern (PDF Card No.: 04-004-8490). For CoPd-CGB, there are two broad peaks for CoPd (111) and CoPd (200) at 40.38° and 47.64° , respectively, consistent with the FCC CoPd reference pattern (PDF Card No.: 04-015-0493). For the CoNiPd-CGB sample, there are two peaks for CoPd (111) and CoPd

(200) at 40.48° and 47.66° , respectively. These peaks are shifted compared to the binary CoPd-CGB. There is an additional peak for FCC CoNi alloy as well. For the ternary CoNiFe-CGB, there are two peaks at 44.46° and 51.78° that are shifted compared to the binary CoNi-CGB. The peak shift also suggests formation of ternary alloys. It should be noted that none of the samples show major peaks below 40° that would correspond to metal oxides. Moreover, in all of these samples, metal nitrates with equal elemental weights were added to the precursor. In all the patterns, the metal peaks are broadened compared to the peaks of unsupported metal nanoparticles produced by the HTRJ. For instance, as shown in **Fig. S5**, the (111) peak of Pd nanoparticles is much sharper than that of Pd-CGBs. This is consistent with growth of much smaller nanoparticles on the GO surface compared to those produced by gas-to-particle conversion in the absence of GO.

Fig. 4 displays Fourier Transform InfraRed (FTIR) and Raman spectra of GO, CGB, and M-CGB. Co-CGB is chosen as an example for M-CGBs. As shown in **Fig. 4a**, FTIR shows a broad O-H stretching peak in 3000 - 4000 cm^{-1} for GO that has disappeared in the CGB sample due to reduction in the HTRJ reactor. Moreover, intensities of peaks

associated with other oxygen-containing functional groups including, C=O stretching and C-O stretching peaks, have been reduced. The FTIR of all M-CGB samples is quite similar to the Co-CGB spectrum with no additional functional groups compared to the CGB. However, there is a minor broad O-H stretching peak in the 3000-4000 cm⁻¹ range which can be due to the adsorption of water or presence of hydroxyl groups on the surface of metal nanoparticles. This is not surprising given the high concentration of water in the reaction chamber. The O-H stretching peak has been observed in our previous flame-synthesized metal nanoparticles as well.³⁰ Raman spectra of GO, CGB, and Co-CGB in **Fig. 4b** show two major peaks at about 1353 and 1597 cm⁻¹ known as the D-band and G-band of carbonaceous materials. The G-band is attributed to sp²-hybridized C atoms, and the D-band is assigned to defects in carbon materials.³¹ For all the samples, the I_D/I_G ratio is below 1 indicating a relatively low concentration of defects in the structures. Due to the reduction of GO in the HTRJ, the I_D/I_G ratio decreased from approximately 0.78 to 0.70. For the Co-decorated sample, the I_D/I_G ratio is around 0.76 suggesting a higher degree of defects in the structure probably due to the introduction of Co nanoparticles.

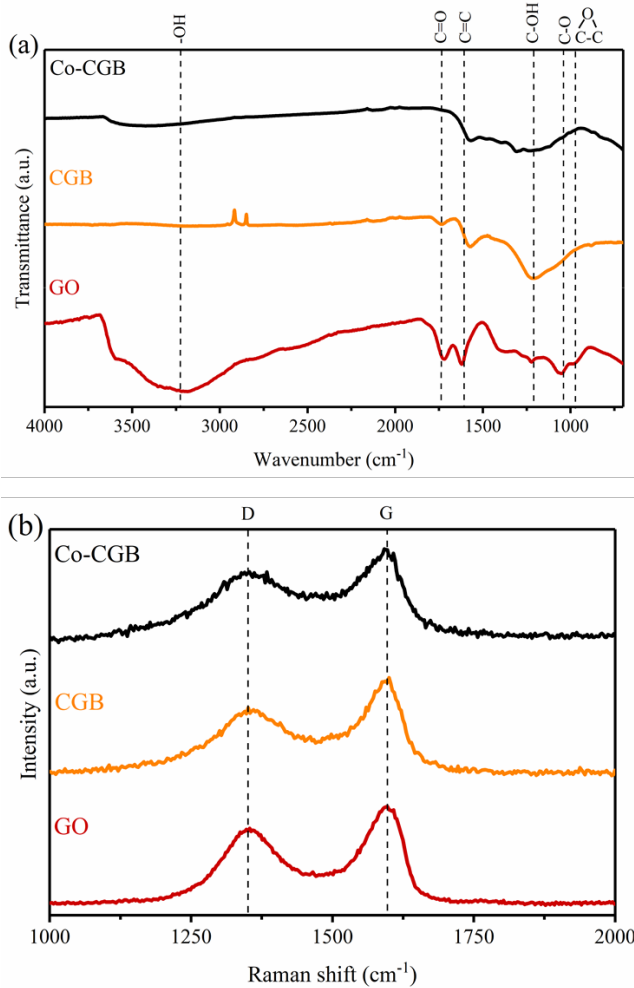


Fig. 4 a) FTIR spectra of GO, CGBs, and cobalt-decorated crumpled graphene ball (Co-CGB); b) Raman patterns of GO, CGB, Co-CGB.

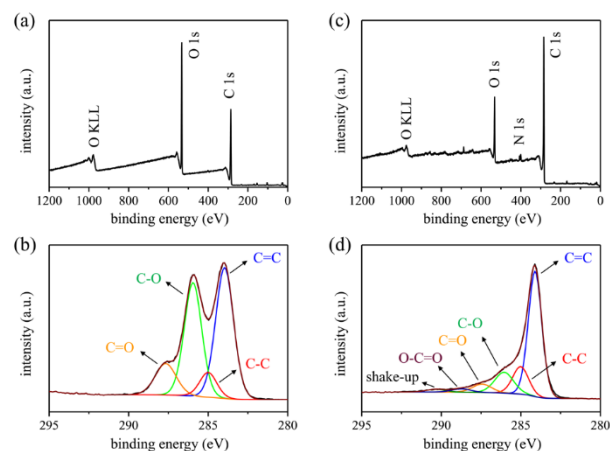


Fig. 5 a) XPS survey scan of GO; b) C 1s spectrum of GO; c) survey scan of CGBs; d) C 1s spectrum of CGB.

The chemical composition and electronic states of GO and CGB samples were investigated by X-ray Photoelectron Spectroscopy (XPS) as shown in **Fig. 5**. For the GO sample, distinct peaks of O KLL, O 1s and C 1s can be observed in the XPS survey spectrum shown in **Fig. 5a**. The high-resolution C 1s spectrum of GO in **Fig. 5b** can be decoupled into 4 bands, corresponding to C=C (284.0 eV), C-C (284.9 eV), C-O (286.5 eV), and C=O (287.6 eV). There is an additional N 1s peak in the XPS survey scan of the CGB (**Fig. 5c**). Nitrogen doping of the CGB is probably due to the presence of nitrogen in the reaction chamber at high temperature. The peak intensity of O 1s in the CGB spectrum is much lower than in the GO spectrum, further confirming the reduction in the HTRJ process. As shown in **Fig. 5d**, oxygen-containing bands in the high-resolution C 1s spectrum of the CGB sample were significantly reduced, verifying the reaction of oxygen with hydrogen in the reactor. However, there are still contributions from O-related species in the spectrum, which suggests that the oxygen-containing groups have not been reduced completely. As shown in **Table S1**, the O/C atomic ratio decreased more than 50% after the reduction of GO in the HTRJ process (from 0.41 in GO to 0.18 in CGB).

Fig. 6 displays XPS spectra of Co, Ni, Pd, and Fe in the M-CGBs. As shown in the high-resolution Co 2p and Ni 2p spectra in **Fig. 6a,b** the spectra can be decoupled into four characteristic peaks ($2p_{1/2}$, $2p_{1/2}$ satellite, $2p_{3/2}$, and $2p_{3/2}$ satellite). The peaks energies are shifted compared to the pure metal binding energies (dashed lines). The shift is attributed to the adsorption of hydroxyl groups and formation of metal hydroxides on bare metal nanoparticles on the surface and few nanometers deep in the M-CGBs. Similar peak positions have been reported for cobalt and nickel hydroxides elsewhere.³²⁻³⁴ The presence of hydroxyl groups was seen in the FTIR spectrum of metal-decorated graphene balls as well. The presence of hydroxyl groups in surface characterization techniques (FTIR and XPS) suggests that the metal nanoparticles in contact with the moist environment in the reaction chamber, adsorb water and form

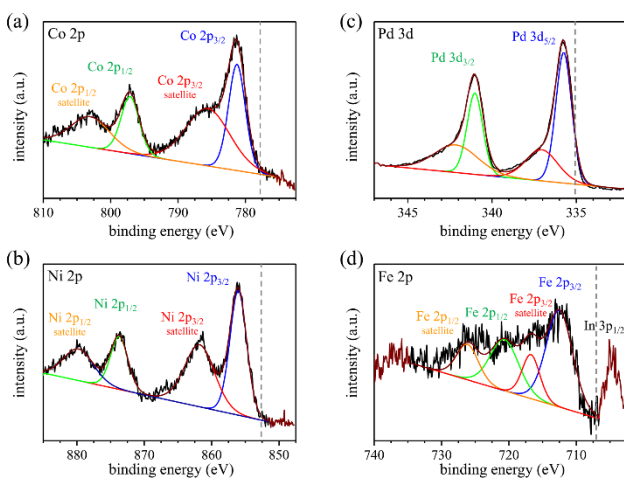


Fig. 6 XPS spectra of: **a**) Co 2p; **b**) Ni 2p; **c**) Pd 3d; and **d**) Fe 2p.

metal hydroxides. **Fig. 6c** provides the high-resolution Pd 3d spectrum. The two characteristic peaks include Pd 3d_{3/2} and Pd 3d_{5/2}. The XPS spectrum of Fe in **Fig. 6d** is noisy probably due to the interference of the indium foil, which has a binding energy close to that of Fe. The peak can be decoupled into four characteristic peaks (2p_{1/2}, 2p_{1/2} satellite, 2p_{3/2}, and 2p_{3/2} satellite). Based on the data provided in **Table S1**, there is a good agreement between the amounts of metal elements added to the precursor and the chemical composition of the product. This further demonstrates that the HTRJ process is capable of producing different transition metal-decorated crumpled reduced graphene oxide nanocomposites with controlled compositions.

Experimental

Materials

Certain commercial equipment, instruments, or materials are identified in this paper in order to specify the experimental procedure adequately. Such identification is not intended to imply recommendation or endorsement by the National Institute of Standards and Technology, nor is it intended to imply that the materials or equipment identified are necessarily the best available for the purpose.

Monolayer GO (GO) water dispersion (4 mg/mL) was purchased from MSE supplies (Tuscon, Arizona). Graphite (powder, <20 µm) was purchased from Millipore-Sigma. Cobalt nitrate hexahydrate (ACROS Organics, 99%), nickel nitrate hexahydrate (ACROS Organics, 99%), ferric nitrate nonahydrate (Fisher Chemical, Certified ACS), and palladium nitrate hydrate (Strem Chemical, Pd ≈40 %, 99.9 %–Pd) were used as metal precursors. Hydrogen (Industrial grade), oxygen (Industrial grade), and liquid nitrogen were obtained from Airgas. A 293 mm polyvinylidene fluoride (PVDF) filter membrane (Millipore-Sigma), 0.22 µm nominal pore size, was used for sample collection.

Synthesis of CGBs and M-CGBs

CGBs and M-CGBs were synthesized via the HTRJ process, as described in detail previously.^{27, 28} In this process, combustion products of a hydrogen-rich flame (H₂: 11 Standard Liters per Minute-SLM, O₂: 3.2 SLM, N₂: 5 SLM) pass through a converging-diverging nozzle. To produce CGBs, an aqueous dispersion of GO (0.5 mg/mL) was injected into the throat section of the nozzle by a syringe pump (Pharmacia P500) at 250 mL/h. To synthesize M-CGBs, metal nitrate precursors (Co, Ni, Fe, Pd) were added to the GO aqueous dispersion. The mass ratio of GO to metal was fixed at 2 for all experiments reported here. For binary and ternary M-CGBs, equal masses of each element were used, keeping the overall GO to metal mass ratio at 2. The aqueous precursor was atomized by the hot high-velocity gas stream and the resulting droplets evaporated in the reducing environment of the reaction chamber containing excess H₂ at high temperature (≈550 °C to 600 °C). After the reaction zone, products were cooled and diluted immediately by mixing with 100 SLM nitrogen, and collected on the filter membrane.

Materials characterizations

The size and morphology of CGBs and M-CGBs were characterized using a JEOL JEM 2010 Transmission Electron Microscope (TEM) at 200 kV working voltage. 200-mesh copper TEM grids with a carbon support film were obtained from Ted Pella. A custom-built electrostatic sampler connected to the HTRJ process was used to collect nanomaterials directly from the aerosol product stream onto TEM grids for offline analysis. Particle size distributions were obtained by TEM image analysis using the Image-J software package. The morphology and elemental composition of nanomaterials were characterized by a Cross-Beam® Focused Ion Beam-Scanning Electron Microscopy (FIB-SEM) Workstation (Carl Zeiss AURIGA) with an Energy Dispersive X-ray Spectroscopy (EDS) detector (Oxford Instruments, X-Max® 20 mm²). The crystal structure of nanomaterials was determined by X-ray Diffraction (XRD) analysis (Bruker Ultima IV with Cu Kα X-ray source). To observe the reduction of GO in the HTRJ and compare the surface functional groups of CGBs and M-CGBs, Fourier Transform InfraRed (FTIR) spectroscopy was performed using a Bruker Vertex 70 spectrometer. The transmittance of each sample was recorded from (700 to 4000) cm⁻¹. X-ray photoelectron spectroscopy (XPS) was used for elemental analysis of CGBs and M-CGBs and to obtain information on the chemical states of the elements in them. XPS measurements were performed using a Kratos AXIS Ultra DLD Spectrometer (Kratos Analytical, Manchester, UK) with a monochromatic Al Kα source (1486.6 eV) operating at 140 W. The base pressure of the sample analysis chamber was ≈ 1.0 × 10⁻⁹ Torr (or 1.33 × 10⁻⁷ Pa), and spectra were collected from a nominal spot size of 300 µm × 700 µm. To facilitate measurements in powder form, the samples were pressed into indium foil, rather than carbon tape, as the carbon signal from the tape would interfere with the carbon signal from the sample. Measurements were

performed in hybrid mode using electrostatic and magnetic lenses, and the pass energy of the analyzer was set at 160 eV for survey scans and 20 eV for high resolution scans, with energy resolutions of 0.5 eV and 0.1 eV. All XPS data analysis was performed using the CasaXPS software package. Raman spectroscopy was employed to determine the structural properties of samples. A Renishaw system with 514 nm excitation laser focused through a 20 \times microscope objective was used at room temperature.

Conclusions

We presented the production of CGBs and M-CGBs using the flame-based HTRJ reactor. Different M-CGBs were synthesized by injecting aqueous solutions containing low-cost metal precursors and dispersed GO into the reactor. M-CGBs include Co-, CoNi-, CoPd-, CoNiFe-, and CoNiPd-CGBs with equal metal weight ratios were produced. According to the TEM images and particle size distributions constructed from them, metal nanoparticles were <4 nm in average size and were well dispersed on the reduced GO sheets. XRD patterns confirmed the formation of non-oxide alloy metal nanoparticles on CGBs. Moreover, crumpled GO sheets were partially reduced, as shown by their XRD and FTIR patterns. Raman spectra showed that the graphitized structure of nanocomposites was preserved after the reduction and metal-decoration. Based on the XPS spectra, more than 50% reduction in oxygen content was observed in CGBs compared to the GO precursor. Moreover, the synthesis of different M-CGBs with controlled compositions was demonstrated. Using the HTRJ process, formation of 3D graphene-based materials and simultaneous decoration with non-oxide transition metal nanoparticles (especially non-noble elements that are hard to reduce in other aerosol-based processes) was possible. These nanocomposites have great potential in various applications where a graphitized carbon supported metal nanomaterial is needed.

Conflicts of interest

There are no conflicts to declare.

Acknowledgements

This work was supported in part by the New York State Center of Excellence in Materials Informatics.

Notes and references

- 1 M. Nazarian-Samani, H.-K. Kim, S.-H. Park, H.-C. Youn, D. Mhamane, S.-W. Lee, M.-S. Kim, J.-H. Jeong, S. Haghigat-Shishavan, K.-C. Roh, S. F. Kashani-Bozorg and K.-B. Kim, *RSC Adv.*, 2016, **6**, 50941-50967.
- 2 L. Jiang and Z. Fan, *Nanoscale*, 2014, **6**, 1922-1945.
- 3 J. Luo, H. D. Jang, T. Sun, L. Xiao, Z. He, A. P. Katsoulidis, M. G. Kanatzidis, J. M. Gibson and J. Huang, *ACS Nano*, 2011, **5**, 8943-8949.
- 4 G.-W. Zhou, J. Wang, P. Gao, X. Yang, Y.-S. He, X.-Z. Liao, J. Yang and Z.-F. Ma, *Ind. Eng. Chem. Res.*, 2012, **52**, 1197-1204.
- 5 B. S. Mao, Z. Wen, Z. Bo, J. Chang, X. Huang and J. Chen, *ACS Appl. Mater. Interf.*, 2014, **6**, 9881-9889.
- 6 S. Mao, Z. Wen, T. Huang, Y. Hou and J. Chen, *Energy Environ. Sci.*, 2014, **7**, 609-616.
- 7 E. Araque, R. Villalonga, M. Gamella, P. Martínez-Ruiz, J. Reviejo and J. M. Pingarrón, *J. Mater. Chem. B*, 2013, **1**.
- 8 J.-Y. Kim, J. Y. Lee, K.-Y. Shin, H. Jeong, H. J. Son, C.-H. Lee, J. H. Park, S.-S. Lee, J. G. Son and M. J. Ko, *Appl Catal. B.*, 2016, **192**, 342-349.
- 9 J.-S. Lee, S.-I. Kim, J.-C. Yoon and J.-H. Jang, *ACS Nano*, 2013, **7**, 6047-6055.
- 10 H. Chen, C. Chen, Y. Liu, X. Zhao, N. Ananth, B. Zheng, L. Peng, T. Huang, W. Gao and C. Gao, *Adv. Energy Mater.*, 2017, **7**.
- 11 B. Yan, X. Li, Z. Bai, Y. Zhao, L. Dong, X. Song, D. Li, C. Langford and X. Sun, *Nano Energy*, 2016, **24**, 32-44.
- 12 H. Wang, L. Shi, T. Yan, J. Zhang, Q. Zhong and D. Zhang, *J. Mater. Chem. A*, 2014, **2**, 4739-4750.
- 13 J. Zheng, H. Liu, B. Wu, Y. Guo, T. Wu, G. Yu, Y. Liu and D. Zhu, *Nano Res.*, 2011, **4**, 705.
- 14 W.-N. Wang, Y. Jiang and P. Biswas, *J. Phys. Chem. Lett.*, 2012, **3**, 3228-3233.
- 15 S. H. Choi and Y. C. Kang, *ChemSusChem*, 2014, **7**, 523-528.
- 16 S. Pratsinis, *Aerosol science and technology: History and reviews*, RTI international, USA, 2011, 475-507.
- 17 R. Koirala, S. E. Pratsinis and A. Baiker, *Chem Soc Rev*, 2016, **45**, 3053-3068.
- 18 S. Gupta, L. Qiao, S. Zhao, H. Xu, Y. Lin, S. V. Devaguptapu, X. Wang, M. T. Swihart and G. Wu, *Adv. Energy Mater.*, 2016, **6**, 1601198.
- 19 I. G. Kim, I. W. Nah, I.-H. Oh and S. Park, *J. Power Sources*, 2017, **364**, 215-225.
- 20 Y. Zhou, X.-C. Hu, Q. Fan and H.-R. Wen, *J. Mater. Chem. A*, 2016, **4**, 4587-4591.
- 21 H. D. Jang, S. K. Kim, H. Chang, J.-W. Choi, J. Luo and J. Huang, *Aerosol Sci Technol.*, 2013, **47**, 93-98.
- 22 Y. Jiang, W.-N. Wang, D. Liu, Y. Nie, W. Li, J. Wu, F. Zhang, P. Biswas and J. D. Fortner, *Environ. Sci. Technol.*, 2015, **49**, 6846-6854.
- 23 C. Lee, S. K. Kim, J.-H. Choi, H. Chang and H. D. Jang, *J. Alloys Compd*, 2018, **735**, 2030-2037.
- 24 Z. Gao, Z. Jin, Q. Ji, Y. Tang, J. Kong, L. Zhang and Y. Li, *Carbon*, 2018, **128**, 117-124.
- 25 C. Lee, E. H. Jo, S. K. Kim, J.-H. Choi, H. Chang and H. D. Jang, *Carbon*, 2017, **115**, 331-337.
- 26 S. Fan, M. Zhao, L. Ding, H. Li and S. Chen, *Biosens Bioelectron*, 2017, **89**, 846-852.
- 27 W. J. Scharmach, R. D. Buchner, V. Papavassiliou, P. Pacouloute and M. T. Swihart, *Aerosol Sci Technol.*, 2010, **44**, 1083-1088.
- 28 M. M. Mohammadi, S. S. Gunturi, S. Shao, S. Konda, R. D. Buchner and M. T. Swihart, *Chem Eng J.*, 2019, **372**, 648-655.
- 29 S. Mao, Z. Wen, H. Kim, G. Lu, P. Hurley and J. Chen, *ACS Nano*, 2012, **6**, 7505-7513.
- 30 S. Konda, M. M. Mohammadi, R. D. Buchner, H. Lin and M. T. Swihart, *AIChE J.*, 2018, **64**, 3826-3834.
- 31 S.-K. Park, J.-S. Park and Y. C. Kang, *ACS Appl. Mater. Interf.*, 2018, **10**, 16531-16540.

- 32 G. Olguin, C. Yacou, S. Smart and J. C. D. da Costa, *Sci. Rep.*, 2013, **3**, 2449-2449.
- 33 G. Mattogno, C. Ferragina, M. A. Massucci, P. Patrono and A. La Ginestra, *J Electron Spectrosc Relat Phenomena.*, 1988, **46**, 285-295.
- 34 A. M. Venezia, R. Bertoncello and G. Deganello, *Surf. Interface Anal.*, 1995, **23**, 239-247.

Supplementary Information for:

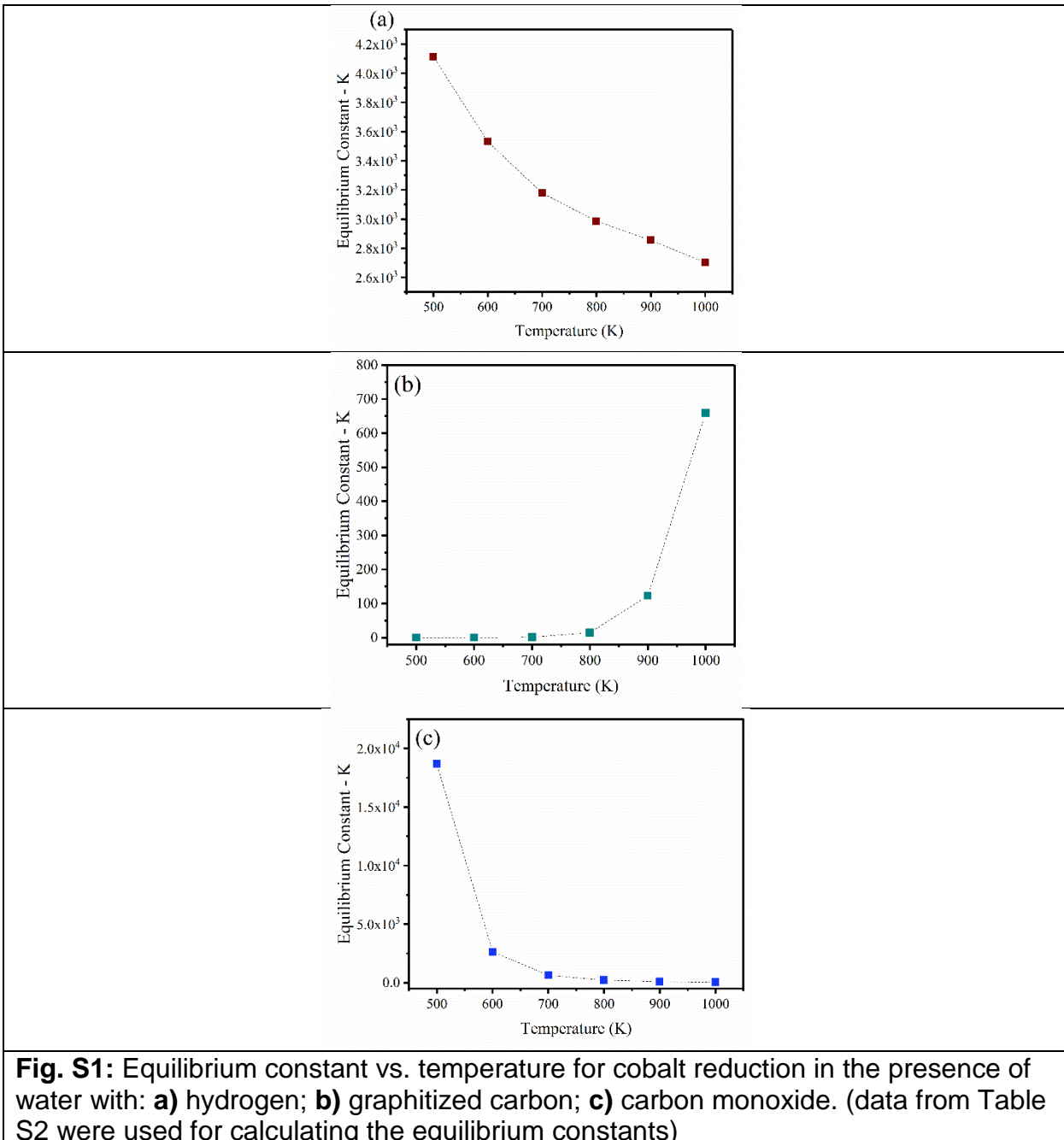
**A general approach to multicomponent metal-decorated
crumpled reduced graphene oxide nanocomposites using a
flame-based process**

Mohammad Moein Mohammadi¹, Shikuan Shao¹, Santosh Srivatsa Gunturi¹, Anirudh Ravi Raghavan¹, Naveshkaanth Alexander¹, Christopher M. Stafford², Raymond D. Buchner¹, Mark T. Swihart^{1}*

¹Department of Chemical and Biological Engineering, University at Buffalo, The State University of New York, Buffalo, NY 14260, USA

²Materials Science and Engineering Division, National Institute of Standards and Technology, Gaithersburg, MD 20899, USA

[*swihart@buffalo.edu](mailto:swihart@buffalo.edu)



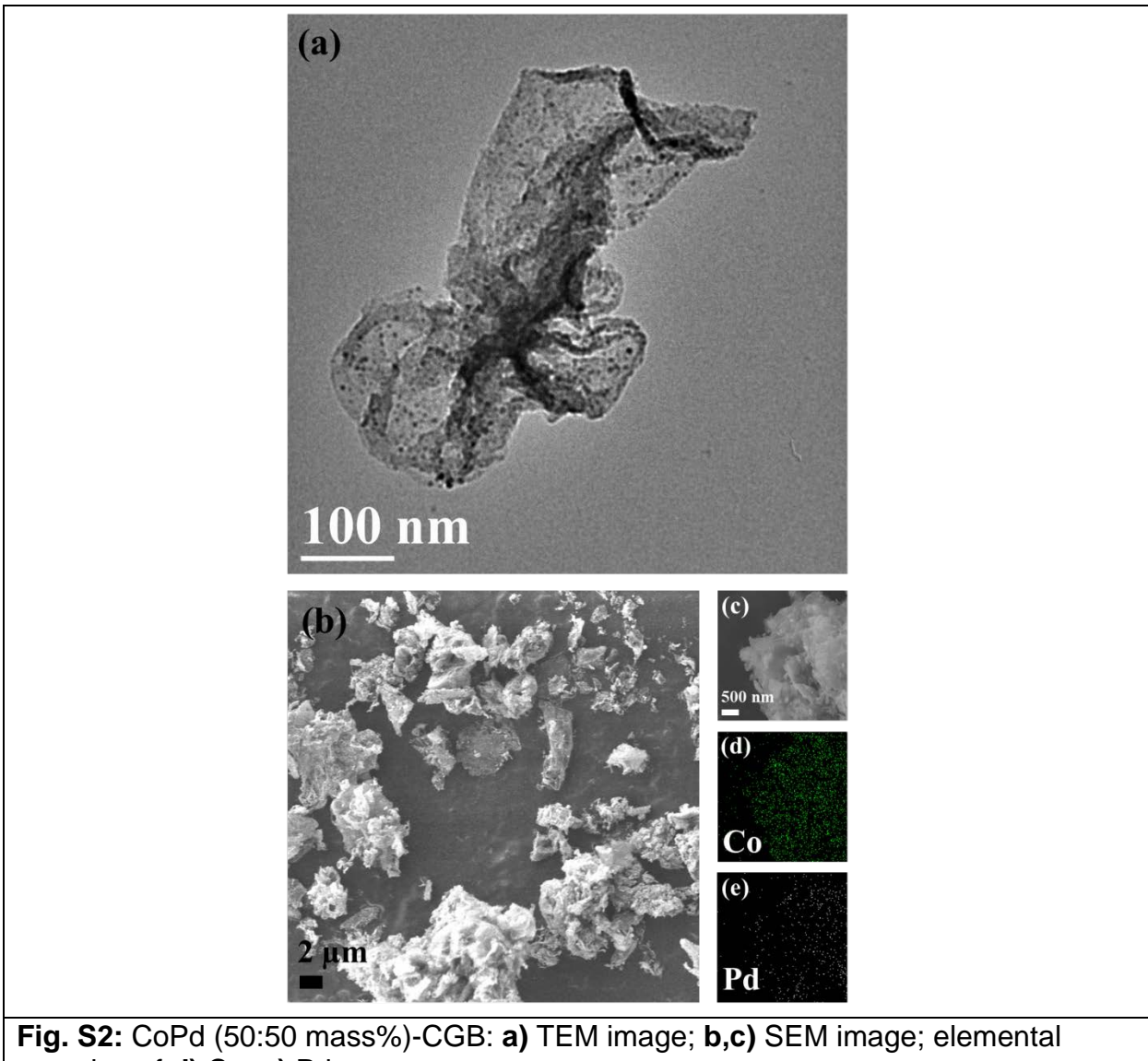


Fig. S2: CoPd (50:50 mass%)-CGB: **a)** TEM image; **b,c)** SEM image; elemental mapping of **d)** Co; **e)** Pd.

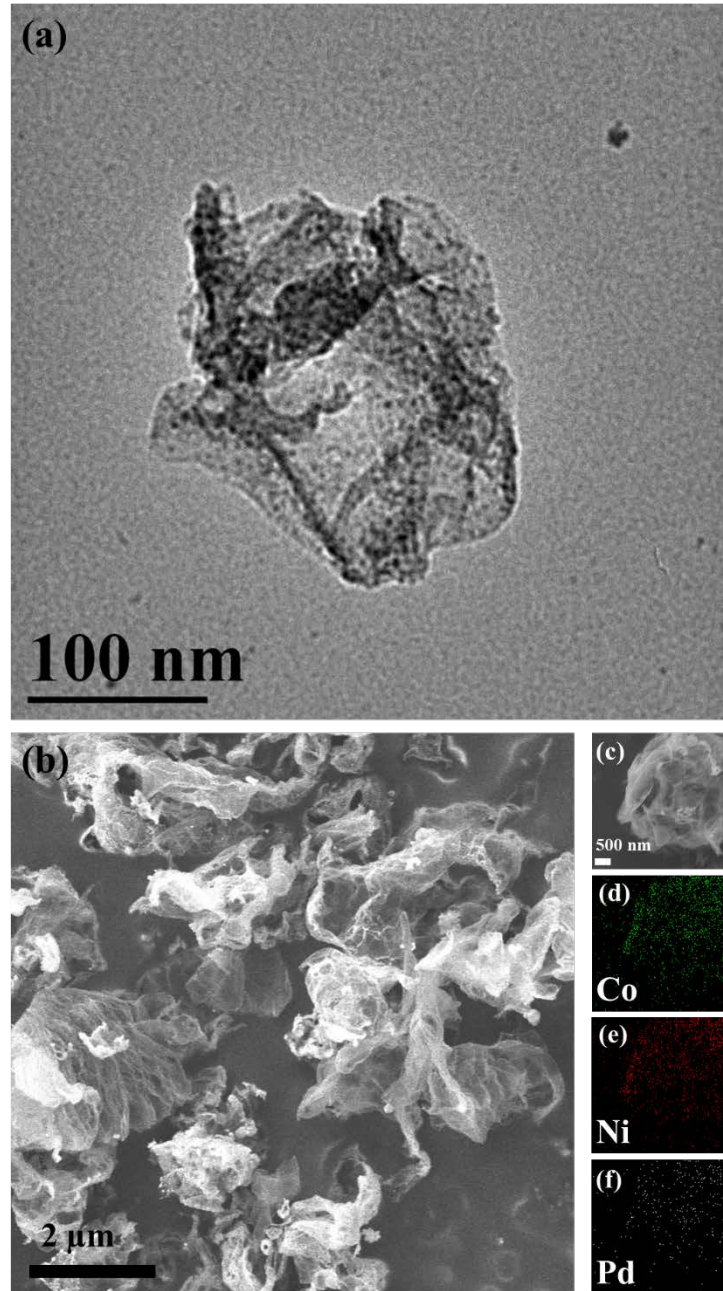


Fig. S3: CoNiPd (33:33:34 mass%)-CGB: **a)** TEM image; **b,c)** SEM image; elemental mapping of **d)** Co; **e)** Ni; **f)** Pd.

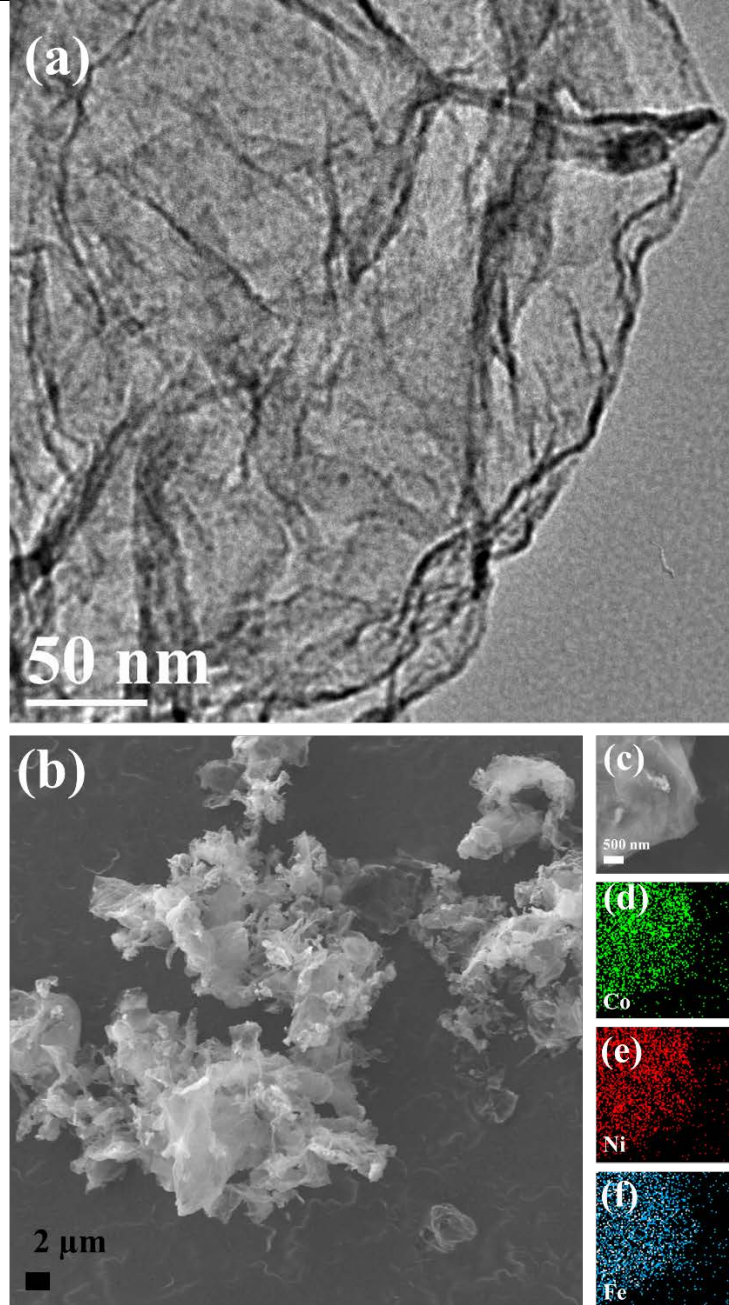


Fig. S4: CoNiFe (33:33:34 mass%)-CGB: **a)** TEM image; **b,c)** SEM image; elemental mapping of **d)** Co; **e)** Ni; **f)** Fe.

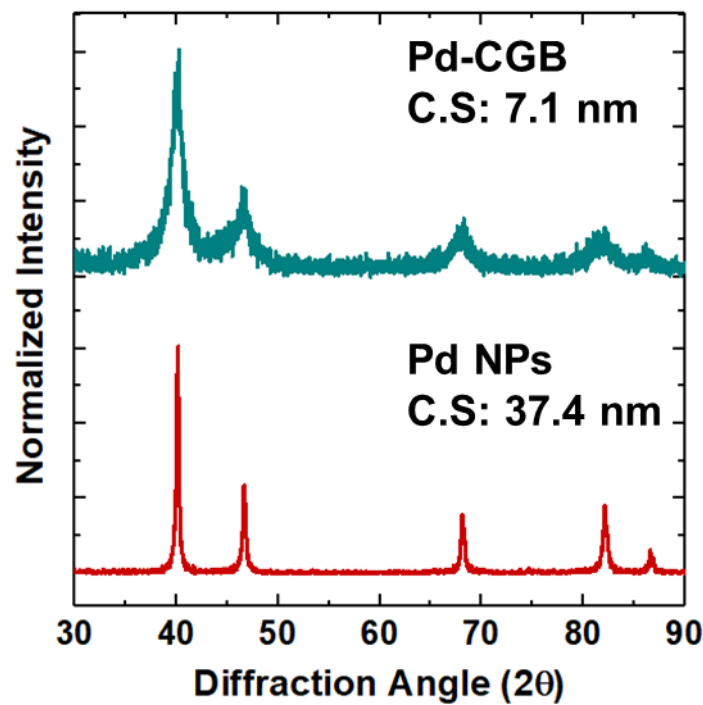


Fig. S5: XRD patterns of Pd-CGB and Pd nanoparticles synthesized using the HTRJ process. (C.S: Crystalline Size)

Table S1. XPS element contents (at. %) of GO, CGB, and M-CGBs

Material	C 1s	O 1s	N 1s	Co 2p	Ni 2p	Pd 3d	Fe 2p
GO	70.30±0.72	29.06±0.92	0.64±0.38	-	-	-	-
CGB	81.37±2.90	15.06±2.42	3.57±0.50	-	-	-	-
CoNi-CGB	59.76±3.18	29.91±5.53	3.51±0.75	3.39±0.88	3.43±1.05	-	-
CoPd-CGB	64.90±6.53	27.26±7.08	1.66±0.56	3.46±0.46	-	2.72±0.53	-
CoNiFe-CGB	58.39±5.88	31.87±4.47	3.63±0.36	2.24±0.37	1.94±0.29	-	1.93±0.89
CoNiPd-CGB	64.04±3.67	26.74±3.65	2.23±0.41	2.91±0.75	2.36±0.41	1.69±0.27	-

*Uncertainties based on mean ±2 standard deviations

Table S2. Phase thermochemistry data for calculating the equilibrium constants of cobalt reduction reactions												
Species	Phase	ΔH_f kJ/mol	Entropy J/(mol K)	Shomate Parameters								
				A	B	C	D	E	F			
CoO	solid	-237.74	52.85	43.65	22.38373	-16.89386	6.556161	0.532263	-249.8643	102.6892	-237.7353	298-1600
Co	solid	0	30.07	10.9943	54.375	-55.5132	25.817	0.164533	-4.7033	30.3258	0	298-700
				-204.576	515.582	-421.55	129.558	17.9267	94.6155	-272.856	0	700-1394
Co	liquid	18	41	45.61355	-3.806989	1.031499	-0.096701	-3.33274	-8.135203	78.01905	18.004	1768. - 3184.943
C	graphite	0	5.6	4.487119045								
CO	gas	-110.53	197.66	25.56759	6.09613	4.054656	-2.671301	0.131021	-118.0089	227.3665	-110.5271	298-1300
CO ₂	gas	-393.52	213.79	24.99735	55.18696	-33.69137	7.948387	-0.13664	-403.6075	228.2431	-393.5224	298-1200
H ₂	gas	0	130.68	33.066178	-11.363417	11.432816	-2.772874	-0.15856	-9.980797	172.707974	0	298-1000
H ₂ O	gas	-241.83	188.84	30.092	6.832514	6.793435	-2.53448	0.082139	-250.881	223.3967	-241.8264	500-1700

Data from: *NIST Chemistry WebBook, SRD 69*. National Institute of Standard and Technology (NIST), U.S. Department of Commerce.